

PAPER

# Large-scale $\text{MoS}_{2(1-x)}\text{Se}_{2x}$ monolayers synthesized by confined-space CVD

To cite this article: Jinming Zhang *et al* 2021 *Nanotechnology* **32** 355601

View the [article online](#) for updates and enhancements.

## You may also like

- [Substrates and interlayer coupling effects on  \$\text{Mo}\_{1-x}\text{W}\_x\text{Se}\_2\$  alloys](#)  
Fang Liang, Hejun Xu, Zuoyuan Dong et al.
- [Rational synthesis of  \$\text{Mo}\_{1-x}\text{W}\_x\text{Y}\_2\$  \(Y = S, Se\) nanowire alloys and their electrochemical catalytic activities](#)  
Lei Yang, Wen Zhang, Ruixin Li et al.
- [Performance tunability of field-effect transistors using  \$\text{MoS}\_{2\(1-x\)}\text{Se}\_{2x}\$  alloys](#)  
Sooraj Sanjay, Kolla Lakshmi Ganapathi, Eswaraiah Varrla et al.



EDINBURGH  
INSTRUMENTS

WORLD LEADING  
MOLECULAR  
SPECTROSCOPY SOLUTIONS



[edinst.com](http://edinst.com)

# Large-scale $\text{MoS}_{2(1-x)}\text{Se}_{2x}$ monolayers synthesized by confined-space CVD

Jinming Zhang<sup>1</sup>, Yezheng Qian<sup>1</sup>, Haiyan Nan<sup>✉</sup>, Xiaofeng Gu and Shaoqing Xiao<sup>\*</sup>

Engineering Research Center of IoT Technology Applications (Ministry of Education), Department of Electronic Engineering, Jiangnan University, Wuxi 214122, People's Republic of China

E-mail: [xiaosq@jiangnan.edu.cn](mailto:xiaosq@jiangnan.edu.cn)

Received 22 December 2020, revised 21 April 2021

Accepted for publication 11 May 2021

Published 7 June 2021



## Abstract

Alloy engineering is efficient in modulating the electronic structure and physical and chemical properties of Transition metal dichalcogenides (TMDs). Here, we develop an efficient and simple confined-space CVD strategy by using a smaller quartz boat nested in a larger quartz boat for the preparation of ternary alloy  $\text{MoS}_{2(1-x)}\text{Se}_{2x}$  monolayers on  $\text{SiO}_2/\text{Si}$  substrates with controllable composition. The effect of hydrogen ratio of the mixed carrier gas ( $\text{Ar}/\text{H}_2$ ) on the resultant flakes are systematically investigated. A hydrogen ratio of 15% is demonstrated to be the most appropriate to synthesize large size (more than  $400\text{ }\mu\text{m}$ ) single crystalline  $\text{MoS}_{2(1-x)}\text{Se}_{2x}$  alloy monolayers. The composition of the alloy can also be changed in a full range ( $2x = 0-2$ ) by changing the weight ratio of Se and S powder. The as-grown monolayer  $\text{MoS}_{2(1-x)}\text{Se}_{2x}$  alloys present continuously high crystal quality in terms of Raman and PL measurements. Furthermore, to visible light (532 nm), the  $\text{MoS}_{2(1-x)}\text{Se}_{2x}$  based photodetectors display wonderful photoresponse with a fast response of less than 50 ms. Our work may be useful in directing the synthesis of TMDs alloys as well as their optoelectronic applications.

Supplementary material for this article is available [online](#)

Keywords: transition metal dichalcogenides, alloy,  $\text{MoS}_{2(1-x)}\text{Se}_{2x}$ , chemical vapor deposition, photodetectors

(Some figures may appear in colour only in the online journal)

## 1. Introduction

The research of two-dimensional materials is promoted by the outstanding chemical and physical properties of graphene and has become the research hotspot in the field of microelectronics [1–4]. Transition metal dichalcogenides (TMDs) and their alloys have attracted much attention in recent years because of their special properties, unique structures and promising application prospects [5–8]. Band gap engineering may be used as a strategy to tune both the optical and electrical properties of the monolayer TMDs as well as to improve the performance of corresponding devices [9–13]. In the practical design of such devices with a wide spectrum

response, excellent flexibility could be provided by using such band gap engineering strategy [14–22]. Take  $\text{MoS}_2$ , for example, tuning of its band gap could make it absorb light within a wider range, adjust its Fermi energy level and improve the performance of its optoelectronic devices [1, 2, 19, 23].

Recently, through the formation of ternary alloys, researchers have successfully adjusted the band gap of monolayer  $\text{MoS}_2$ . In fact, because  $\text{MoS}_{2(1-x)}\text{Se}_{2x}$  monolayers have a wide range of tunable band gap, as well as tunable optical and electronic properties, they can be widely used in photodetectors and super capacitors [15]. These alloys also exhibit better performance than their binary compounds in terms of electrochemical properties such as energy storage and conversion [24]. Umrao *et al* reported the growth of large-area monolayer  $\text{MoS}_{2(1-x)}\text{Se}_{2x}$  alloys using a low-

<sup>1</sup> These authors contributed equally to this work.

\* Author to whom any correspondence should be addressed.

pressure CVD method. However, the band gap was only tuned from 1.77 to 1.69 eV, corresponding to a wavelength adjustment from 700 to 734 nm [18]. Zhang *et al* developed a one-step CVD strategy to successfully synthesize  $\text{MoS}_{2(1-x)}\text{Se}_{2x}$  monolayer alloys with a full tuning of the band gap photoluminescence (PL) from 1.83 eV (for ML- $\text{MoS}_2$ ) to 1.55 eV (for ML- $\text{MoSe}_2$ ). However, the size of the monolayer alloys are only up to 100  $\mu\text{m}$  [21]. Yang *et al* have achieved the large-area synthesis of high-quality  $\text{MoS}_{2(1-x)}\text{Se}_{2x}$  monolayer alloys with a full tuning of the band gap and a size coverage of hundreds of microns by using a CVD strategy with  $\text{H}_2/\text{Ar}$  mixed carrier gas [20]. However, the effect of  $\text{H}_2$  ratio has not been well studied and the optoelectronic properties of such alloy monolayers has not been investigated.

In our recent works, we have developed a confined-space CVD strategy to achieve high-quality and large-size  $\text{MoS}_2$  [25],  $\text{MoSnS}_2$  [3] and  $\text{ReSSe}$  [26] monolayer films on amorphous  $\text{SiO}_2/\text{Si}$  substrates. The designed confined-space constructed by two stacking substrates or two boats nested within each other cause a remarkable reduction in the concentration and flow rate of the reactants inside the confined reaction room, thereby decreasing the nucleation density and growth rate [26, 27]. Furthermore, the confined-space CVD provides a relatively stable microgrowth environment with the improved control of the precursor supply and carrier gas transport [28]. All these positive effects jointly contribute to the synthesis of high-quality TMD crystals with large size and good uniformity. In this work, the confined-space CVD strategy with  $\text{H}_2/\text{Ar}$  mixed carrier gas is also shown to be applicable for the synthesis of large size  $\text{MoS}_{2(1-x)}\text{Se}_{2x}$  monolayers on  $\text{SiO}_2/\text{Si}$  substrates. We systematically study the effect of  $\text{H}_2$  ratio on the size of the resultant monolayer flakes. The maximum size is up to 400  $\mu\text{m}$  when the  $\text{H}_2$  ratio is set at 15%, which is a breakthrough in size compared to previous work [4, 16–18, 20, 21, 29, 30]. The Se composition ( $2x$ ) can be varied in a wide range (0–2) by adjusting the mass ratio of Se and S powder sources as confirmed by x-ray photoelectron spectroscopy (XPS). Raman and PL mapping results reveal the uniform distribution of Mo, S, and Se elements in the  $\text{MoS}_{2(1-x)}\text{Se}_{2x}$  monolayer alloys. The optoelectronic performances of the  $\text{MoS}_{2(1-x)}\text{Se}_{2x}$  based photodetectors exhibit a minimum response time of 22 ms.

## 2. Experiment

### 2.1. Synthesis of $\text{MoS}_{2(1-x)}\text{Se}_{2x}$ alloys

Figure 1(a) shows the schematic of the confined-space CVD system. The whole process was carried out in a dual-zone horizontal quartz tube furnace consisting of heating zone 1 (upstream) and heating zone 2 (downstream), where the supply rate of chalcogenide compounds and molybdenum oxide powders were independently controlled. A quartz boat loaded with sulfur powder (99.5%) was placed in the center of heating zone 1, while another boat loaded with selenium powder (99.5%) powder was placed next to the first one.

Meanwhile, a smaller quartz boat loaded with  $\text{MoO}_3$  powder nested in a third quartz boat with the same size as the first and second ones was placed in the center of heating zone 2. The Si wafers with 285 nm  $\text{SiO}_2$  ( $\text{SiO}_2/\text{Si}$ ) were placed on top of the smaller boat facing down above the  $\text{MoO}_3$  powder. The smaller quartz boat nested in a larger quartz boat and covered by the Si wafer formed a relatively confined-space, as clearly shown in figure S1 (available online at [stacks.iop.org/NANO/32/355601/mmedia](https://stacks.iop.org/NANO/32/355601/mmedia)). Before the experiment, ultra-high purity argon (99.99%) gas with a flow rate of 200 sccm was introduced into the quartz tube for 10 min to remove pollution sources. Then, a mixed  $\text{Ar}/\text{H}_2$  gas was maintained at a flow rate of 50 sccm to serve as the carrier gas during the whole growth process. Within 60 min, the two heating zones of the furnace were heated to target temperatures (250 °C for S and Se, 780 °C for the  $\text{MoO}_3$ ). The reaction time was set to 20 min, followed by natural cooling. The temperature curve is given in figure S2. The  $\text{Ar}/\text{H}_2$  mixed gas flow rate was set to 50 sccm during the CVD process.

### 2.2. Synthesis of $\text{MoS}_2$ and $\text{MoSe}_2$

The synthesis of both  $\text{MoS}_2$  and  $\text{MoSe}_2$  monolayers was similar to that of  $\text{MoS}_{2(1-x)}\text{Se}_{2x}$ , except the growth temperatures. For  $\text{MoS}_2$ , the growth temperature was set at 720 °C and the Se powder in the heating zone 1 needs to be removed. In contrast, the growth temperature of  $\text{MoSe}_2$  became 750 °C and only the Se powders remained in the heating zone 1. Other parameters were consistent with that for the growth of  $\text{MoS}_{2(1-x)}\text{Se}_{2x}$ .

### 2.3. Fabrication of photoconductive devices

The photodetector devices based on  $\text{MoS}_{2(1-x)}\text{Se}_{2x}$  alloys were fabricated using standard electron beam lithography. 50 nm thick Au deposited by thermal evaporation was used to serve as electrical contacts for the  $\text{MoS}_{2(1-x)}\text{Se}_{2x}$  based photodetector. Aimed to get the spectral photocurrent response, we measured the electrical and photoresponse characteristics of related devices using a Keithley 2643B analyzer under dark and illuminated conditions in atmosphere environment. A 532 nm laser (RENISHAW RL 532C50) was employed. For all the photocurrent measurements in this experiment, the lasers were focused on the sample with a 50 $\times$  objective (NA = 0.5) and the size of the light spot is about 1  $\mu\text{m}$ . It means that the device channel length is much bigger than the light spot. We made the power of the illuminated laser under change with the help of optical attenuators and recorded the time-dependent photoresponse using a chopper with a frequency of 1 Hz.

### 2.4. Characterization

By OM (Leica DM2700M), the surface morphologies of monolayer  $\text{MoS}_{2(1-x)}\text{Se}_{2x}$  alloys could be characterized. We used a Renishaw LabRAM Invia micro-Raman system with 532 nm excitation laser to measure the Raman spectra characterizations in an atmospheric environment at room temperature. We employed the same Raman system to take PL

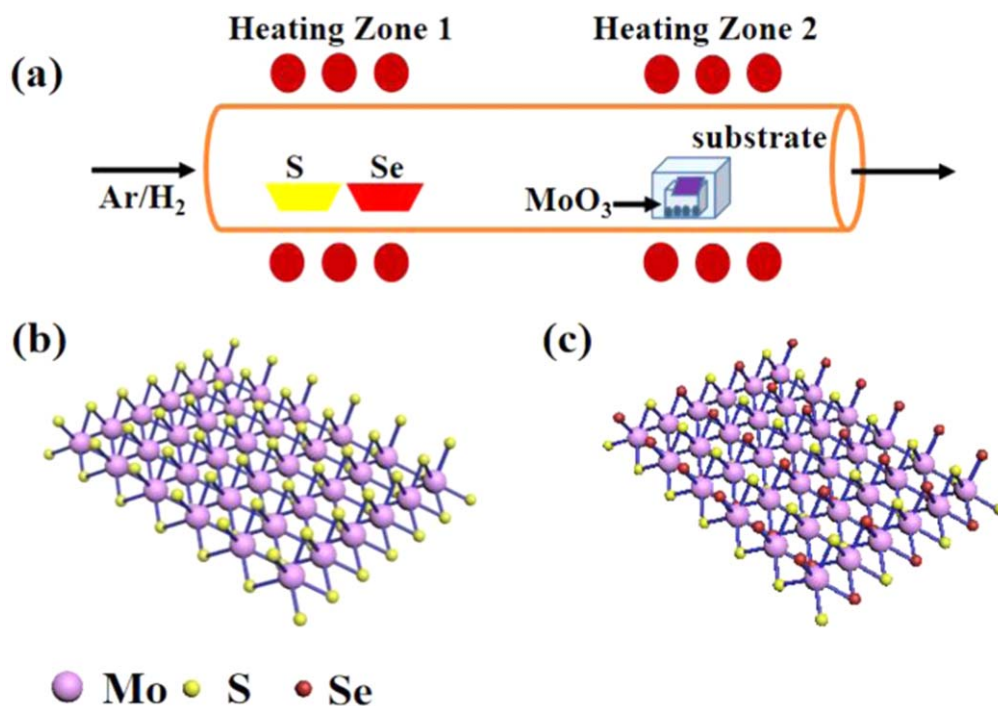


**Figure 1.** (a) Schematic of the confined-space CVD system for the growth of  $\text{MoS}_{2(1-x)}\text{Se}_{2x}$  monolayers. (b), (c) Atomic structures of  $\text{MoS}_2$  and  $\text{MoS}_{2(1-x)}\text{Se}_{2x}$ .

measurements which demonstrate the band structure of  $\text{MoS}_{2(1-x)}\text{Se}_{2x}$  with a tunable band gap. The thickness of monolayer  $\text{MoS}_{2(1-x)}\text{Se}_{2x}$  alloys was measured by AFM (Bruker model: Dimension ICON). The elemental composition of the alloys was identified by XPS (Thermo Scientific Escalab 250Xi).

### 3. Results and discussion

In figures 1(b) and (c), the optimized atomic structures of the  $\text{MoS}_2$  and  $\text{MoS}_{2(1-x)}\text{Se}_{2x}$  alloy monolayers are shown, respectively. In the *X*-direction and *Y*-direction, the monolayers own periodicity. For  $\text{MoS}_2$ , nearly perfect hexagonal symmetry can be found, a Mo atom is orderly wrapped by 6 S atoms. Since  $\text{MoS}_2$  has the same structure as  $\text{MoSe}_2$ , doping elements have a very slight effect on the hexagonal lattice structure [5, 6, 31]. Figure S3 compares the experimental results between the common CVD and the confined-space CVD. For the common CVD, inhomogeneous and unclear  $\text{MoS}_{2(1-x)}\text{Se}_{2x}$  domains with coexistence of monolayers and thick flakes are obtained on  $\text{SiO}_2/\text{Si}$  substrates due to the uncontrolled nucleation density and growth rate. In contrast, for the confined-space CVD, high-quality  $\text{MoS}_{2(1-x)}\text{Se}_{2x}$  monolayer crystals with large size and good uniformity are synthesized on the  $\text{SiO}_2/\text{Si}$  substrate.

Compared with S element, the chemical activity of Se element is very low and requires a reducing agent to help promote the reaction [2, 5, 16, 22, 32, 33].  $\text{H}_2$  is often used to serve as the reducing agent when using a CVD system to synthesize Se-based TMDC (such as  $\text{WSe}_2$  and  $\text{MoSe}_2$ ). Though the lack of  $\text{H}_2$  may not result in the synthesis of Se-

based or Te-based TMDC samples, excessive  $\text{H}_2$  may make the metal oxide (like  $\text{MoO}_3$ ) precursor become metal through reduction and thus degrade the evaporation rate of the oxide precursor, thereby making it hard to achieve large TMDC monolayer samples [34]. In addition, the use of  $\text{H}_2$  has also been proved to have benefits because of its ability to prevent the remaining oxygen from oxidizing the growing flakes.

Therefore, carrier gas composition ( $\text{Ar}/\text{H}_2$  ratio) must be optimized before the composition control of monolayer alloys. We kept the total gas flow rate ( $\text{Ar}+\text{H}_2$ ) unchanged at 50 sccm and growth parameters under same growth conditions (1 g Se, 0.5 g S and 780 °C) while varying the  $\text{H}_2$  percentage values ( $P = 100\% \times \text{H}_2/(\text{Ar}+\text{H}_2)$ ) including 3%, 5%, 15%, 20%, 25% and 30%. The optical image of the resultant sample at  $P = 3\%$  is shown in figure 2(a). One can observe that the surface coverage of the sample remains low and the sample is covered with many thick layers that fail to undergo surface epitaxial growth due to insufficient ion sources provided by hydrogen. With the increase in hydrogen ratio to 5% (figure 2(b)), the produced flakes are mainly consisting of triangle monolayers with an average size of about 100  $\mu\text{m}$  due to the increasing reducing environment but some sporadically distributed thick layers can still be observed. When the hydrogen ratio further increases to 10%, the resultant flakes are quite homogeneous and all consisting of triangle monolayers with an average size of about 150  $\mu\text{m}$  (figure 2(c)). When hydrogen ratio is further increased to 15%, the resultant flakes are similar to that obtained at  $P = 15\%$  but with a maximum size of more than 400  $\mu\text{m}$  and the average size can reach up to 200  $\mu\text{m}$ . However, when the  $\text{H}_2$  ratio rises to 20% or beyond (25%), the resultant triangle flakes is getting denser and denser both the size is getting



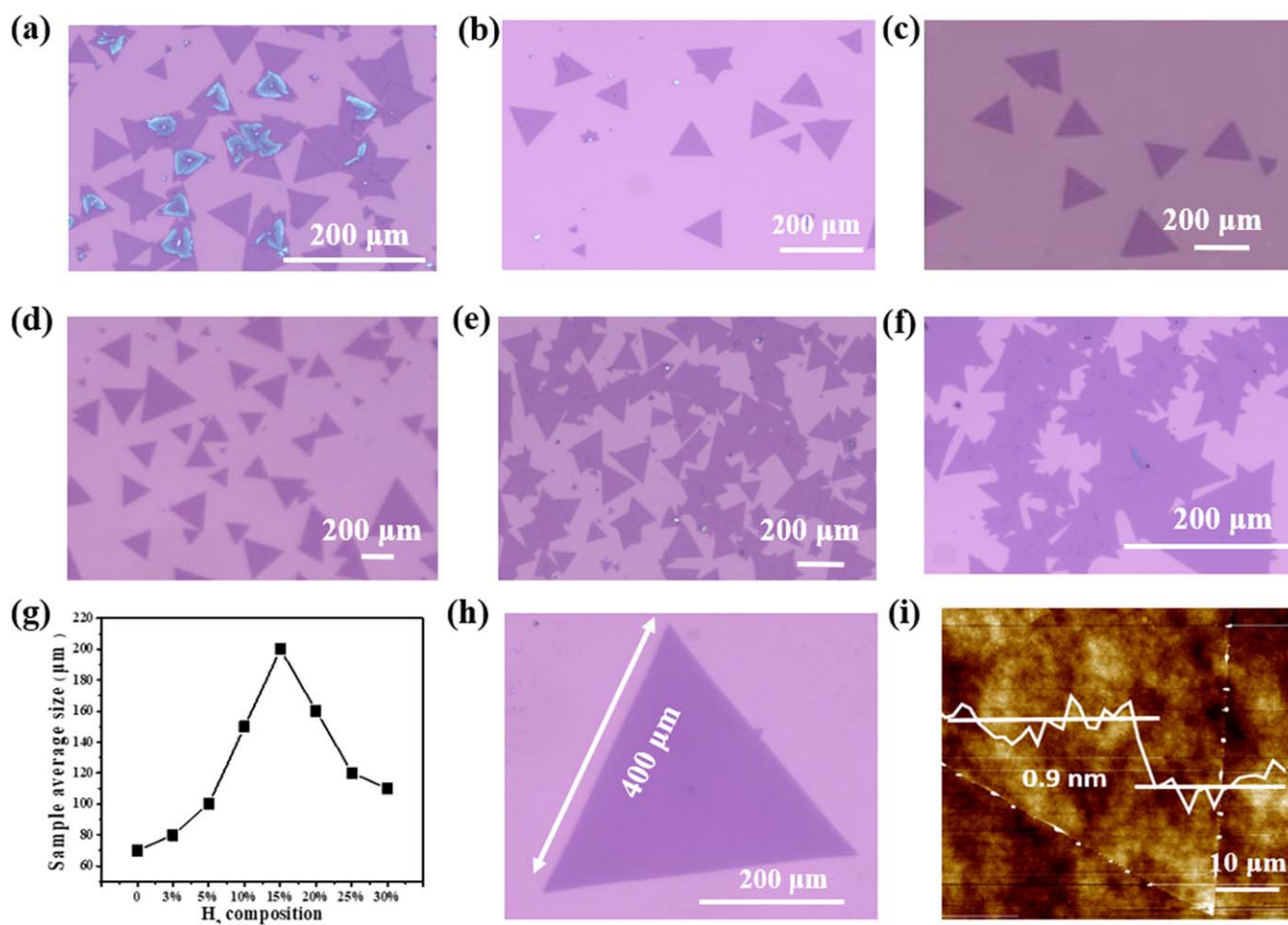


**Figure 2.** OM of MoS<sub>2</sub>(1-x)Se<sub>2x</sub> grown at different hydrogen concentrations: (a) 3%, (b) 5%, (c) 10%, (d) 15%, (e) 20% and (f) 25%. (g) The statistical distribution of the average size of the samples grown at different hydrogen concentrations. (h) A typical OM of the sample with a maximum size of more than 400 μm growth at hydrogen concentration of 15%. (i) A typical AFM image of the monolayer alloy.

smaller (figure 2(c) at  $P = 20\%$ ), and some of them even merge together to form a continuous poly-crystalline film (figure 2(d) at  $P = 25\%$ ). This is because more H<sub>2</sub> may result in more MoO<sub>3-x</sub> steam, which would lead to more nucleation centers on the growth substrate and thus producing the resultant flakes as observed.

Figure 2(d) depicts the statistical variation trend of the average size of the resultant MoS<sub>2</sub>(1-x)Se<sub>2x</sub> flakes as a function of the hydrogen concentration. With the increase in hydrogen concentration, the flake size first slowly increases to a saturated value and then begins to decline. In addition, it has been also reported that excessive H<sub>2</sub> can etch monolayer crystal after its formation. Therefore, we take  $P = 15\%$  as the optimum carrier gas composition for the growth of MoS<sub>2</sub>(1-x)Se<sub>2x</sub> alloy monolayers with tunable composition. A typical enlarged image of the flake with the maximum size of more than 400 μm is presented in figure 2(e). The monolayer nature of the alloys is confirmed by AFM measurements as shown in figure 2(f).

In order to obtain MoS<sub>2</sub>(1-x)Se<sub>2x</sub> alloy monolayers with a wide Se composition from 0 to 2, we adjusted the mass ratio of Se and S powder sources but kept the total weight of Se and S powders at 1.5 g. The chemical composition of the as-

grown MoS<sub>2</sub>(1-x)Se<sub>2x</sub> alloy monolayers was analyzed by XPS and a typical result is shown in figure 3. One can observe from figure 3(a) the appearances of Mo, S and Se elements in the alloys, just like the Si and O element signals that come from the SiO<sub>2</sub>/Si substrate. For this sample, the atomic compositions of Mo, S, and Se are respectively calculated to be 9.18%, 16.78%, and 6.64%, indicating that this alloy sample is MoS<sub>1.44</sub>Se<sub>0.56</sub>. The high-resolution spectra of Mo 3d, S 2p, and Se 3d are also displayed in figures 3(b)–(d), respectively. The strong peaks located at nearly 228.1 and 231.3 eV represent the Mo 3d<sub>5/2</sub> and Mo 3d<sub>3/2</sub>, respectively. While the two peaks at nearly 53.5 and 54.3 eV could be ascribed to Se 3d<sub>5/2</sub> and Se 3d<sub>3/2</sub>, and S 2p<sub>3/2</sub> and S 2p<sub>1/2</sub> states locate at binding energies of 161.1 and 162.5 eV. Both the Mo and S element peaks of the alloy monolayer sample shift slightly toward lower energy, in comparison with those of pure MoS<sub>2</sub> monolayer sample, which could be attributed to the addition of Se atoms. This keeps consistency for the other monolayer MoS<sub>2</sub>(1-x)Se<sub>2x</sub> alloys. As shown in figure S4, with the gradual increase of Se composition ( $x$ ) in monolayer MoS<sub>2</sub>(1-x)Se<sub>2x</sub> alloys, the Se 3p peaks appear and their intensities show a monotonous increase, while S 2p peaks

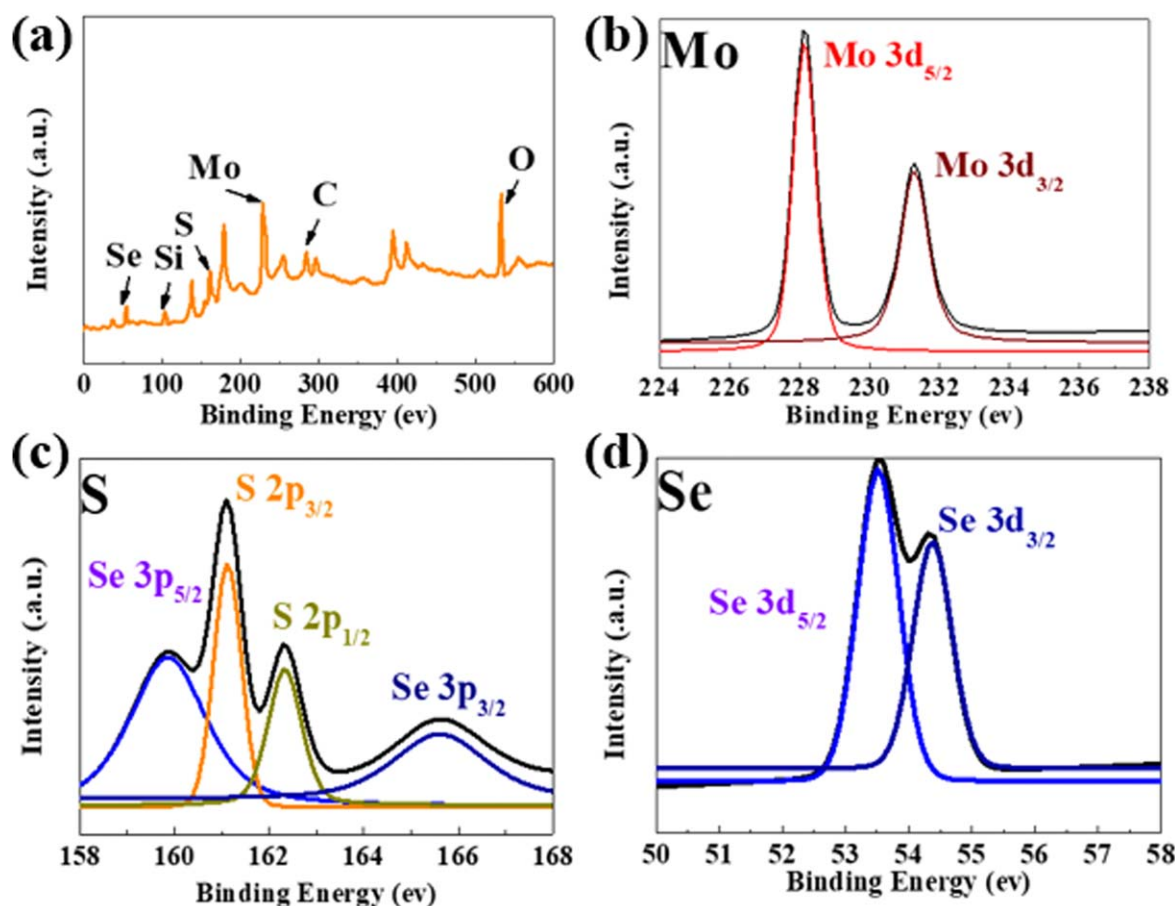


**Figure 3.** XPS full spectrum (a) and high-resolution spectra of Mo 3d (b), S 2p (c), and Se 3d (d) of the  $\text{MoS}_{1.44}\text{Se}_{0.56}$  alloy monolayers grown on  $\text{SiO}_2/\text{Si}$  substrate.

become gradually more and more insignificant until they finally disappear.

The dependence of Raman and PL spectra on the Se composition ( $2x$ ) of the  $\text{MoS}_{2(1-x)}\text{Se}_{2x}$  alloys is shown in figures 4(a) and (b), respectively. The PL and Raman behaviors related to Se composition are summarized in figure 4(c). Two characteristic Raman vibration modes that appear at nearly  $383$  and  $403\text{ cm}^{-1}$  for monolayer  $\text{MoS}_2$ , are representative of the in-plane vibration mode ( $E_{2g}$ ) and the out of plane vibration mode ( $A_{1g}$ ). We calculated the relative peak distances between the  $E_{2g}$  and  $A_{1g}$  modes, which is a key indicator to determine the number of  $\text{MoS}_2$  layers. The calculated relative peak distances of our  $\text{MoS}_2$  is  $20\text{ cm}^{-1}$ , confirming the nature of monolayer [8]. For pure  $\text{MoSe}_2$ , the out-plane vibration mode ( $A_{1g}\text{-MoSe}_2$ ) and the in-plane vibration mode ( $E_{2g}\text{-MoSe}_2$ ) locate at  $240$  and  $280\text{ cm}^{-1}$ , respectively. As the Se composition in the monolayer  $\text{MoS}_{2(1-x)}\text{Se}_{2x}$  alloys increases, the  $E_{2g}\text{-MoS}_2$  and  $A_{1g}\text{-MoS}_2$  modes shift to low frequency slowly. Three identical sublayers form the Monolayer  $\text{MoS}_2$ , and two planes of S atoms sandwich one layer of Mo atoms, as shown in figure 1. Six S atoms are bonded with one Mo atom and form symmetrical six Mo–S bonds. Three Mo–S bonds are below the Mo atom plane, while the others are above the Mo atom plane. When part of the S sites are replaced by Se atoms, the introduction of Se atoms causes local distortion due to their larger atomic

radius, meaning the destruction of the original symmetry of the  $\text{MoS}_2$ . Without doubt, the bond length of the original Mo–S and Mo–Mo bond would be changed by this distortion changes. Hence, the atomic vibrations of the  $E_{2g}$  and  $A_{1g}$  modes of  $\text{MoS}_2$  are softened by an external tensile strain. As the Se composition in the monolayer  $\text{MoS}_{2(1-x)}\text{Se}_{2x}$  alloys increases, the tensile strain has a synchronous increase, causing the red shifts in the  $E_{2g}\text{-MoS}_2$  and  $A_{1g}\text{-MoS}_2$  modes. At the same time, the  $E_{2g}\text{-MoSe}_2$  and  $A_{1g}\text{-MoSe}_2$  modes appear and gradually becomes dominant.

The PL peaks also display obvious red shift with increasing Se composition. We can observe a PL emission peak located at  $680\text{ nm}$  for pure monolayer  $\text{MoS}_2$ , which mainly originates from A-exciton emission and shows a direct band gap of  $1.82\text{ eV}$ . Such direct exciton transition occurs at the same K point between the conduction band minimum (CBM) and the valence band maximum (VBM) in the Brillouin zone. As we know, in monolayer  $\text{MoS}_2$ , the  $d_z^2$  orbital of Mo cations and the  $p_x, p_y$  orbitals of S anions are the main part of CBM state, while the VBM state is mainly composed of the  $d_{x-y}$  and  $d_{xy}$  orbitals of Mo cations and the  $p_x, p_y$  orbitals of S anions [18, 20, 21, 23, 35–38]. The band gap of monolayer  $\text{MoS}_2$  is determined by the nonbonding  $d$  band structure [18, 20, 21, 23, 35]. For example, the band gap of the monolayer  $\text{MoS}_2$  is mostly determined by the gap size that between the  $d_z^2$  orbital of Mo cations that is fully occupied

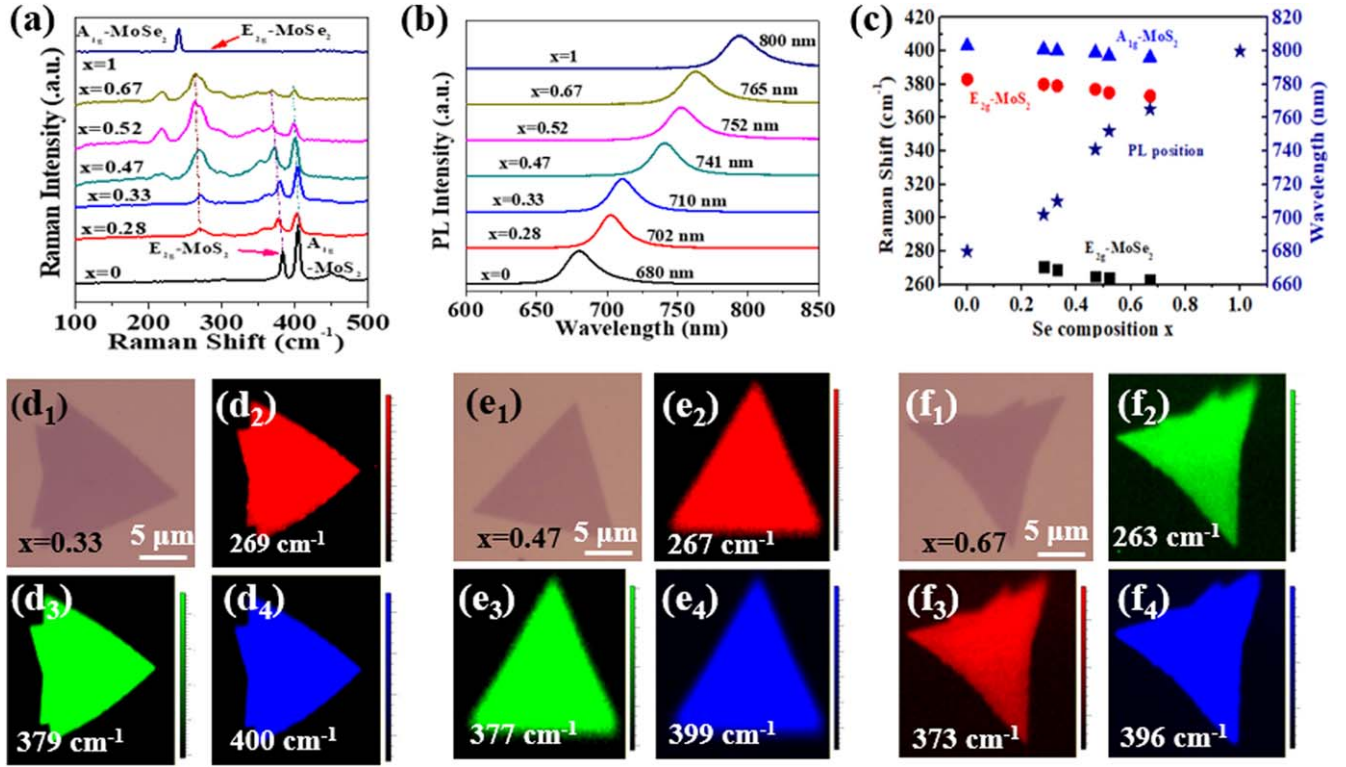


**Figure 4.** (a) Raman spectra of monolayer MoS<sub>2</sub>(1-x)Se<sub>2x</sub> alloys with different Se composition; (b) PL spectra measured from monolayer MoS<sub>2</sub>(1-x)Se<sub>2x</sub> alloys with different Se composition; (c) the selected Raman frequency, Raman intensity and PL peak positions of different alloys which corresponding to E<sub>2g</sub>-MoS<sub>2</sub>, A<sub>1g</sub>-MoS<sub>2</sub> and E<sub>2g</sub>-MoSe<sub>2</sub> modes, respectively; (d1)–(f1) OM, (d2)–(f2) frequency-selected Raman mappings of E<sub>2g</sub>-MoS<sub>2</sub> mode, (d3)–(f3) frequency-selected Raman mappings of E<sub>2g</sub>-MoS<sub>2</sub> mode; (d4)–(f4) frequency-selected Raman mappings of A<sub>1g</sub>-MoS<sub>2</sub> mode which belong to three selected MoS<sub>2</sub>(1-x)Se<sub>2x</sub> alloys with different Se composition:  $x = 0.33, 0.47$  and  $0.67$ .

and the empty  $d_{x-y}^2, d_{xy}$  orbitals of the same one. When S atoms are replaced by Se atoms, the electronegativity value for Se atoms is 2.4 which is undoubtedly lower than that of 2.5 for S atoms, so it makes the bonding between Mo and Se more powerful. The fully occupied  $d_z^2$  band directly broadens because of the more powerful bonding mode. Between the fully occupied  $d_z^2$  band and the neighboring empty band, a decreased gap size is obtainable with the increasing Se composition. Thus, the size of the direct band gap begins to monotonously reduce [20]. A minimum at 1.55 eV (800 nm) can be achieved for pure MoSe<sub>2</sub>, as shown in figures 4(b) and (c). As a result, we have achieved monolayer MoS<sub>2</sub>(1-x)Se<sub>2x</sub> alloys with a wide Se composition from 0 to 2, corresponding to the PL peak position from 680 nm (1.82 eV) for pure MoS<sub>2</sub> to intermediate value for MoS<sub>2</sub>(1-x)Se<sub>2x</sub> and finally to 800 nm (1.82 eV) for MoSe<sub>2</sub>.

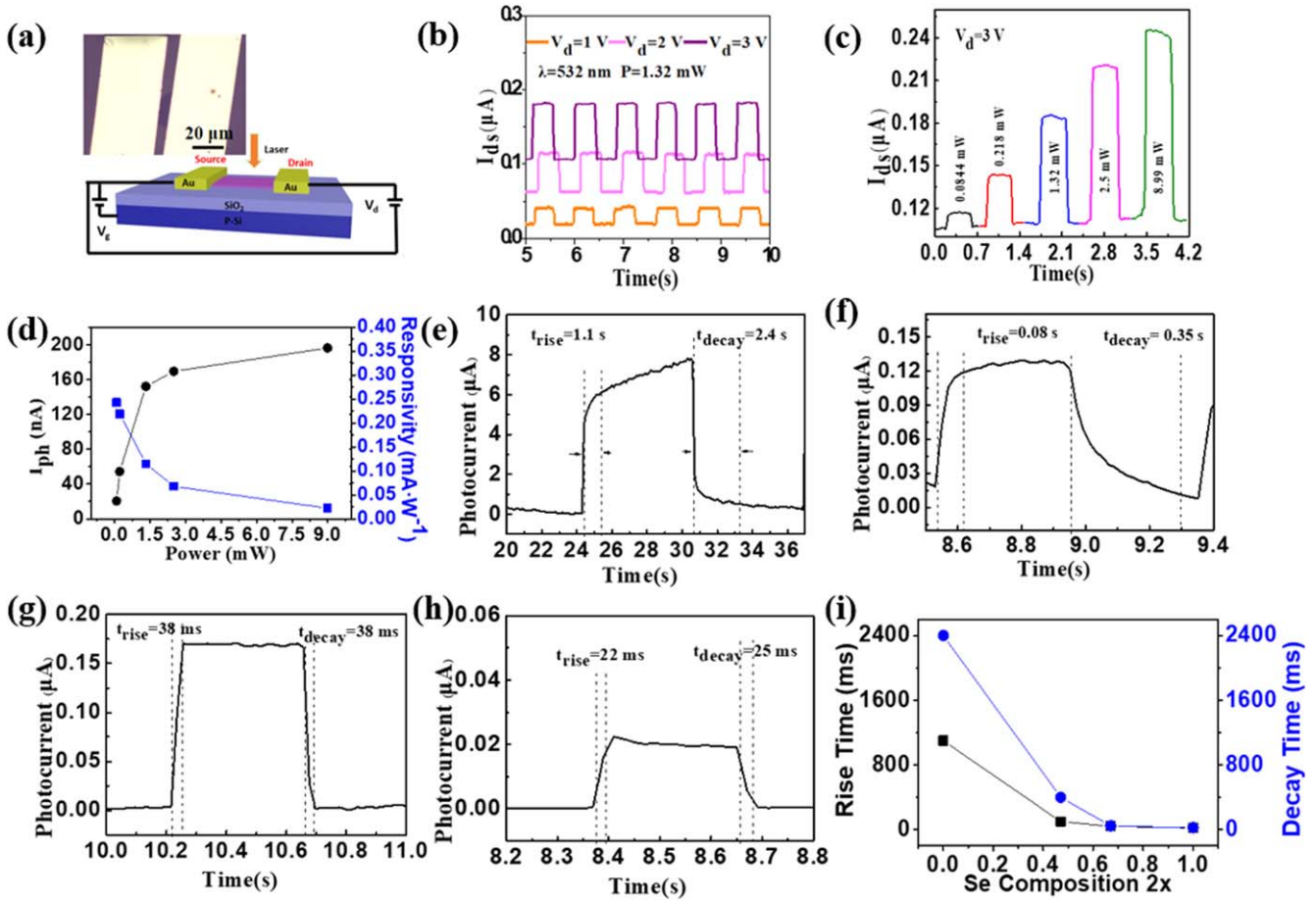
Figures 4(d)–(f) shows the optical images of frequency-selected Raman mappings, that are collected from three samples with different Se composition ( $x = 0.33, 0.47$ , and  $0.67$ ). The Raman mappings of E<sub>2g</sub>-MoSe<sub>2</sub>, A<sub>1g</sub>-MoS<sub>2</sub> and E<sub>2g</sub>-MoS<sub>2</sub> modes are all bright and distinct in the contrast between the sample region (colorful area) and the surrounding substrate region (dark area), obviously reflecting the uniformity of S and Se compositions distribution in the sample domain.

Figure 5(a) is a schematic image of a typical photodetector based on monolayer MoS<sub>2</sub>(1-x)Se<sub>2x</sub> alloys. Under the

same light source with the wavelength of 532 nm and constant light power of 1.32 mW, we measure the drain-source current ( $I_{ds}$ ) versus time plots, unless noted specially. Figures 5(b) and (c) show the tested performance of a photodetector based on MoS<sub>0.66</sub>Se<sub>1.34</sub> alloys under different drain-source voltage ( $V_{ds}$ ) and different incident laser power, respectively. When the photodetector is illuminated by the laser, the drain-source current ( $I_{ds}$ ) quickly increases to a saturated state. When turning off the laser, it restores the original level immediately. We can obviously observe from figure 5(b) that three stages namely rise state, stable state, and decay state constitute to each switching cycle of the device. We could regularly switch the  $I_{ds}$  between the high and low states immediately by turning on or off the light source. In addition, the light current ( $I_{ill}$ ) shows a significant increase with the monotonic increase of the  $V_{ds}$  from 1 to 3 V. The light current ( $I_{ill}$ ) as a function of the  $V_{ds}$  is shown in figure S5, showing a nonlinear behavior. This may be due to the poor contact as well as the heating effect of the long time illumination. Likewise, as the incident laser power increases, the light current ( $I_{ill}$ ) also increases significantly. The curves of photocurrent ( $I_{ph}$ ) and photoresponsivity ( $R$ ) as a function of the incident laser power are given in figure 5(d). The  $I_{ph}$  and  $R$  are usually defined as

$$I_{ph} = I_{ill} - I_{dark}, \quad (1)$$





**Figure 5.** Optoelectronic properties of the MoS<sub>2</sub>(1-x)Se<sub>2x</sub> photodetectors. (a) Schematic diagram of the MoS<sub>0.66</sub>Se<sub>1.34</sub> based photodetector. (b) Drain-source current  $I_{ds}$  as a function of time with laser switched on/off at  $V_{ds} = 1, 2$  and 3 V under the 532 nm laser illumination. (c) Rise or decay characteristics of the photocurrent with the laser illumination switched on and off under illumination with different laser power. (d) Photocurrent and photoresponsivity as a function of incident power for the MoS<sub>0.66</sub>Se<sub>1.34</sub> based photodetector. (e)–(f) The time-dependent photoresponse characteristics of the MoS<sub>2</sub>(1-x)Se<sub>2x</sub> based devices with different Se composition at  $V_{ds} = 3$  V: (e) MoS<sub>2</sub>, (f) MoS<sub>1.06</sub>Se<sub>0.94</sub>, (g) MoS<sub>0.66</sub>Se<sub>1.34</sub> and (h) MoSe<sub>2</sub>. (i) The plots of rise and decay times measured as a function of Se composition ( $x = 0, 0.47, 0.67$  and 1).

$$R = \frac{I_{ph}}{P}, \quad (2)$$

where  $I_{ill}$ ,  $I_{dark}$ , and  $P$  represent the light current, dark current, and incident power, respectively. With the incident laser power, the photocurrent has a monotonous increase, so it can be known that photocarriers mostly determine the photoresponse.

The capability of photodetector devices to follow a fast-switching optical signal is determined by the response time, thus, it is an important factor for photodetectors. Figures 5(e)–(h) present the normalized temporal photoresponse characteristic of the photodetectors based on MoS<sub>2</sub>, MoS<sub>1.06</sub>Se<sub>0.94</sub>, MoS<sub>0.66</sub>Se<sub>1.34</sub> and MoSe<sub>2</sub> monolayers. Between 10% and 90% of the increasing and decreasing photocurrents, we extract the rising and decaying time values. The relationship between the deduced rising and decaying times and the Se composition is plotted as a line graph in figure 5(i), exhibiting a monotonic decrease from  $\approx 1100$  to  $\approx 22$  ms and from  $\approx 2400$  to  $\approx 25$  ms, respectively, with the increase in Se composition from 0 to 2. These response time values are competitive to those of the reported photodetectors based on Mo-based TMDs [39–42].

We make an inference that the response time would greatly reduce once the Se elements are incorporated into such Mo-based TMDC alloys. The Se composition can modulate defect-induced trap states and makes the response time reduce. The detrapping time of carriers from a deep trap would be exponentially prolonged than the ones in shallow traps, thus longer decay/response time is expected for the photodetectors where the deep trap dominates the channel material. In such Mo-based TMDC alloys, the S ingredient plays the role of an n-type dopant while the Se one acts as a p-type dopant. With the Se composition increases, p-type doping gets more dominant and make the quasi-Fermi level for holes move down. At last, the shallow level traps are in a dominant position compared with the negligible contribution from the deep ones, so the response rate would get a significant improvement [1, 4, 11, 12, 20, 29, 30, 37, 43–45].

#### 4. Conclusion

In summary, we have developed a confined-space CVD scheme by using a maller quartz boat nested in a larger quartz



boat for the successful synthesis of single crystalline  $\text{MoS}_{2(1-x)}\text{Se}_{2x}$  alloy monolayers with large-area and high uniformity. The effect of hydrogen ratio of the mixed carrier gas ( $\text{Ar}/\text{H}_2$ ) on the resultant flakes are systematically investigated. A hydrogen ratio of 15% is demonstrated to be the most appropriate to synthesize large size (more than  $400\ \mu\text{m}$ ) single crystalline  $\text{MoS}_{2(1-x)}\text{Se}_{2x}$  alloy monolayers. By adjusting the mass ratio of Se and S powder sources, the Se composition can be continually modulated in a full range from 0 to 2, corresponding to  $\text{MoS}_2$  to  $\text{MoS}_{2(1-x)}\text{Se}_{2x}$  and finally to  $\text{MoSe}_2$ , as confirmed by XPS, Raman and PL studies. The  $\text{MoS}_{2(1-x)}\text{Se}_{2x}$  based photodetectors also exhibit a good photoresponse to visible light (532 nm) with a response time of less than 30 ms. This work may provide reference value for latecomers in the field of CVD synthesis of two-dimensional materials as well as their optoelectronic applications.

## Acknowledgments


This work is partially supported by the National Nature Science Foundation under Grants 62074070 and 11704159, the Natural Science Foundation of Jiangsu Province, China under Grant BK20170167, the Fundamental Research Funds for the Central Universities of China under Grants JUSRP221015, the 111 Project under Grant B12018.

## Data availability statement

All data that support the findings of this study are included within the article (and any supplementary files).

## ORCID iDs

Haiyan Nan  <https://orcid.org/0000-0002-1445-8472>

Shaoqing Xiao  <https://orcid.org/0000-0002-0564-5532>

## References

- [1] Li S Y *et al* 2019 Enhanced performance of a CVD  $\text{MoS}_2$  photodetector by chemical *in situ* N-type doping *ACS Appl. Mater. Interfaces* **11** 11636–44
- [2] Lu X *et al* 2014 Large-area synthesis of monolayer and few-layer  $\text{MoSe}_2$  films on  $\text{SiO}_2$  substrates *Nano Lett.* **14** 2419–25
- [3] Mo H X, Zhang X M, Liu Y, Kang P P, Nan H Y, Gu X F, Ostrikov K K and Xiao S Q 2019 Two-dimensional alloying molybdenum tin disulfide monolayers with fast photoresponse *ACS Appl. Mater. Interfaces* **11** 39077–87
- [4] Rajbanshi B, Sarkar S and Sarkar P 2015 the electronic and optical properties of  $\text{MoS}_{2(1-x)}\text{Se}_{2x}$  and  $\text{MoS}_{2(1-x)}\text{Te}_{2x}$  monolayers *Phys. Chem. Chem. Phys.* **17** 26166–74
- [5] Shaw J C, Zhou H L, Chen Y, Weiss N O, Liu Y, Huang Y and Duan X F 2014 Chemical vapor deposition growth of monolayer  $\text{MoSe}_2$  nanosheets *Nano Res.* **7** 511–7
- [6] Shi R *et al* 2020 Oxide inhibitor-assisted growth of single-layer molybdenum dichalcogenides ( $\text{Mo}_x\text{S}_2$ ,  $X = \text{S}, \text{Se}, \text{Te}$ ) with controllable molybdenum release *ACS Nano* **14** 7593–601
- [7] Sial M N, Usman M, Moghaddam A N, Channa A I, Yu Y N, Qing F Z and Ji H N 2019 CVD-Grown 2D molybdenum diselenide: morphology, spectroscopic and mechanical characterization *J. Alloys Compd.* **803** 795–803
- [8] Bosi M and Rotunno E 2019 Direct synthesis of few-layer  $\text{MoS}_2$  on silica nanowires by chemical vapor deposition *Nanosci. Nanotechnol.* **19** 4323–5
- [9] Lopez-Posadas C B, Wei Y X, Shen W F, Kahr D, Hohage M and Sun L D 2019 Direct observation of the CVD growth of monolayer  $\text{MoS}_2$  using *In Situ* optical spectroscopy *Beil. Nanotechnol.* **10** 557–64
- [10] Hyun C M, Choi J H, Lee S W, Park J H, Lee K T and Ahn J H 2018 Synthesis mechanism of  $\text{MoS}_2$  layered crystals by chemical vapor deposition using  $\text{MoO}_3$  and sulfur powders *J. Alloys Compd.* **765** 380–4
- [11] Chen L, Shi M T, He B H, Zhou M J, Xu C X, Chen Z G and Kuang Y F 2019 Effect of two-step doping pathway on the morphology, structure, composition, and electrochemical performance of three-dimensional n,S-codoped graphene framework *Mater. Res.* **34** 1993–2002
- [12] Hosseini S S and Adelifard M 2020 The effect of multi-walled carbon nanotubes and reduced graphene oxide doping on the optical and photovoltaic performance of  $\text{Ag}_2\text{BiI}_5$ -based solar cells *Electron Mater.* **49** 5790–800
- [13] Yang L, You X C, Sheng Z Y, Ma D R, Yu D Q, Xiao X and Wang S 2018 The promoting effect of noble metal (Rh, Ru, Pt, Pd) doping on the performances of  $\text{MnOx-CeO}_2/\text{graphene}$  catalysts for the selective catalytic reduction of NO with  $\text{NH}_3$  at low temperatures *New J. Chem.* **42** 11673–81
- [14] Wang B B, Qu X L, Zheng K, Levchenko I, Keidar M, Zhu M K, Xu S and Ostrikov K 2017 C And O doped bn nanoflake and nanowire hybrid structures for tuneable photoluminescence *J. Alloys Compd.* **705** 691–9
- [15] Bay M, Ozden A, Ay F and Perkgoz N K 2019 Bandgap tuning of monolayer  $\text{MoS}_{2(1-x)}\text{Se}_{2x}$  alloys by optimizing parameters *Mater. Sci. Semicond. Process.* **99** 134–9
- [16] Feng Q L, Mao N N, Wu J X, Xu H, Wang C M, Zhang J and Xie L M 2015 Growth of  $\text{MoS}_{2(1-x)}\text{Se}_{2x}$  ( $x = 0.41\text{--}1.00$ ) monolayer alloys with controlled morphology by physical vapor deposition *ACS Nano* **9** 7450–5
- [17] Gong Q F, Cheng L, Liu C H, Zhang M, Feng Q L, Ye H L, Zeng M, Xie L M, Liu Z and Li Y G 2015 Ultrathin  $\text{MoS}_{2(1-x)}\text{Se}_{2x}$  alloy nanoflakes for electrocatalytic hydrogen evolution reaction *ACS Catal.* **5** 2213–9
- [18] Umrao S, Jeon J, Jeon S M, Choi Y J and Lee S 2017 A homogeneous atomic layer  $\text{MoS}_{2(1-x)}\text{Se}_{2x}$  alloy prepared by low-pressure chemical vapor deposition and its properties *Nanoscale* **9** 594–603
- [19] Wang J, Lin X Y, Zhang R X, Chu Z Y and Huang Z Y 2018 Transition metal dichalcogenides  $\text{MX}_2$  ( $M = \text{Mo}, \text{W}; X = \text{S}, \text{Se}, \text{Te}$ ) and  $\text{MX}_2\text{-CIP}$  composites: promising materials with high microwave absorption performance *J. Alloys Compd.* **743** 26–35
- [20] Yang L, Fu Q, Wang W H, Huang J, Huang J L, Zhang J Y and Xiang B 2015 Large-area synthesis of monolayered  $\text{MoS}_{2(1-x)}\text{Se}_{2x}$  with a tunable band gap and its enhanced electrochemical catalytic activity *Nanoscale* **7** 10490–7
- [21] Zhang W T, Li X D, Jiang T T, Song J L Q, Lin Y, Zhu L X and Xu X L 2015 CVD synthesis of  $\text{Mo}_{(1-x)}\text{W}_x\text{S}_2$  and  $\text{MoS}_{2(1-x)}\text{Se}_{2x}$  alloy monolayers aimed at tuning the bandgap of molybdenum disulfide *Nanoscale* **7** 13554–60
- [22] Fu Q, Yang L, Wang W H, Han A, Huang J, Du P W, Fan Z Y, Zhang J Y and Xiang B 2015 Synthesis and enhanced electrochemical catalytic performance of monolayer

- WS<sub>2(1-x)</sub>Se<sub>2x</sub> with a tunable band gap *Adv. Mater.* **27** 4732–8
- [23] Klee V et al 2015 Superlinear composition-dependent photocurrent in CVD-grown monolayer MoS<sub>2(1-x)</sub>Se<sub>2x</sub> alloy devices *Nano Lett.* **15** 2612–9
- [24] Cai G H, Peng L, Ye S Y, Huang Y C, Wang G F and Zhang X J 2019 Defect-rich MoS<sub>2(1-x)</sub>Se<sub>2x</sub> few-layer nanocomposites: a superior anode material for high-performance lithium-ion batteries *J. Mater. Chem. A* **7** 9837–43
- [25] Zhang X M, Nan H Y, Xiao S Q, Wan X, Ni Z H, Gu X F and Ostrikov K 2017 Shape-uniform, high-quality monolayered MoS<sub>2</sub> crystals for gate-tunable photoluminescence *ACS Appl. Mater. Interfaces* **9** 42121–30
- [26] Kang P P, Han H Y, Zhang X M, Mo H X, Ni Z H, Gu X F, Ostrikov K and Xiao S Q 2019 Controllable synthesis of crystalline ReS<sub>2(1-x)</sub>Se<sub>2x</sub> monolayers on amorphous SiO<sub>2</sub>/Si substrates with fast photoresponse *Adv. Opt. Mater.* **8** 1901415
- [27] Zhang X M, Xiao S Q, Shi L H, Nan H Y, Wan X, Gu X F, Ni Z H and Ostrikov K 2018 Large-size Mo<sub>1-x</sub>W<sub>x</sub>S<sub>2</sub> and W<sub>1-x</sub>Mo<sub>x</sub>S<sub>2</sub> ( $x = 0-0.5$ ) monolayers by confined-space chemical vapor deposition *Appl. Surf. Sci.* **457** 591–7
- [28] Chen C C, Kuo C J, Liao C D, Chang C F, Tseng C A, Liu C R and Chen Y T 2015 Growth of large-area graphene single crystals in confined reaction space with diffusion-driven chemical vapor deposition *Chem. Mater.* **27** 6249–58
- [29] Yin W X, He D, Bai X and Yu W W 2019 Synthesis of tungsten disulfide quantum dots for high-performance supercapacitor electrodes *J. Alloys Compd.* **786** 764–9
- [30] Hou K Q, Huang Z Y, Liu S Q, Qiao G C H, Li H X and Qi X 2020 A hydrothermally synthesized MoS<sub>2(1-x)</sub>Se<sub>2x</sub> alloy with deep-shallow level conversion for enhanced performance of photodetectors *Nanoscale Adv.* **2** 2185–91
- [31] Yin H, Zhang X D, Lu J W, Geng X M, Wan Y F, Wu M Z and Yang P 2020 Substrate effects on the CVD growth of MoS<sub>2</sub> and WS<sub>2</sub> *Mater. Sci.* **55** 990–6
- [32] Hwang Y and Shin N 2019 Hydrogen-assisted step-edge nucleation of MoSe<sub>2</sub> monolayers on sapphire substrates *Nanoscale* **11** 7701–9
- [33] Zhao Y, Lee H, Choi W, Fei W D and Lee C J 2017 Large-area synthesis of monolayer MoSe<sub>2</sub> films on SiO<sub>2</sub>/Si substrates by atmospheric pressure chemical vapor deposition *RSC Adv.* **7** 27969–73
- [34] Zhang Y et al 2013 Controlled growth of high-quality monolayer WS<sub>2</sub> layers on sapphire and imaging its grain boundary *ACS Nano* **7** 8963–71
- [35] Yue Y C, Feng Y Y, Chen J C, Zhang D H and Feng W 2017 Two-dimensional large-scale bandgap-tunable monolayer MoS<sub>2(1-x)</sub>Se<sub>2x</sub>/graphene heterostructures for phototransistors *J. Mater. Chem. C* **5** 5887–96
- [36] Tian X N, Jiang Z Q, Shuang X N, Gu X W, Maiyalagan T and Jiang Z J 2020 Insight into the effects of microstructure and nitrogen doping configuration for hollow graphene spheres on oxygen reduction reaction and sodium-ion storage performance *Int. J. Hydrog. Energy* **45** 16569–82
- [37] Li Y C, Li X and Xu Y T 2017 Theoretical insights into the effect of pristine, doped and hole graphene on the overall performance of dye-sensitized solar cells *Inorg. Chem. Front.* **7** 157–68
- [38] Yao W W, Kang Z L, Deng J J, Chen Y, Song Q, Ding X L, Lu F C and Wang W J 2020 Synthesis of 2D MoS<sub>2(1-x)</sub>Se<sub>2x</sub> semiconductor alloy by chemical vapor deposition *RSC Adv.* **10** 42172–7
- [39] Liu X K, Hu S Q, Lin Z C, Li X H, Song L J, Yu W J, Wang Q and He W 2021 High-performance MoS<sub>2</sub> photodetectors prepared using a patterned gallium nitride substrate *ACS Appl. Mater. Interfaces* **13** 15820–6
- [40] Li Z W, Wu J, Wang C, Zhang H, Yu W J, Lu Y M and Liu X K 2020 High-performance monolayer MoS<sub>2</sub> photodetector enabled by oxide stress liner using scalable chemical vapor growth method *Nanophotonics* **9** 1981–91
- [41] Kang Z, Cheng Y F, Zheng Z, Cheng F, Chen Z Y, Li L Y, Tan X Y, Xiong L, Zhai T Y and Gao Y H 2019 MoS<sub>2</sub>-Based Photodetectors Powered by Asymmetric Contact Structure with Large Work Function Difference *Nano-Micro Letters* **11** 34
- [42] Chang Y H et al 2014 Monolayer MoSe<sub>2</sub> grown by chemical vapor deposition for fast photodetection *ACS Nano* **8** 8582–90
- [43] Liu F, Zhu G Q, Yang D Z, Jia D, Jin F M and Wang W 2019 Systematic exploration of N, C configurational effects on the orr performance of Fe–N doped graphene catalysts based on DFT calculations *RSC Adv.* **9** 22656–67
- [44] Jing M H, Xu Z Y, Fang D W, Fan X Z, Liu J G and Yan C W 2019 Anchoring effect of the partially reduced graphene oxide doped electrospun carbon nanofibers on their electrochemical performances in vanadium flow battery *J. Power Sources* **425** 94–102
- [45] Zhang X, Zhang Z H and Zhou Z 2018 MXene-based materials for electrochemical energy storage *Energy Chem.* **27** 3–85